AD_____

Award Number: DAMD17-99-1-9429

TITLE: Automatic Exposure Control Device for Digital Mammography

PRINCIPAL INVESTIGATOR: Laurie L. Fajardo, M.D.

CONTRACTING ORGANIZATION: Johns Hopkins University
Baltimore, MD 21218

REPORT DATE: August 2001

TYPE OF REPORT: Annual

PREPARED FOR: U.S. Army Medical Research and Materiel Command
Fort Detrick, Maryland 21702-5012

REPORT DOCUMENTATION PAGE

Form Approved
OMB No. 074-0188

1. AGENCY USE ONLY (Leave blank)	2. REPORT DATE	3. REPORT TYPE AND DATES COVERED
	August 2001	Annual (1 Aug 00 - 31 Jul 01)

4. TITLE AND SUBTITLE
Automatic Exposure Control Device for Digital Mammography

5. FUNDING NUMBERS
DAMD17-99-1-9429

6. AUTHOR(S)
Laurie L. Fajardo, M.D.

7. PERFORMING ORGANIZATION NAME(S) AND ADDRESS(ES)
Johns Hopkins University
Baltimore, MD 21218

E-Mail: LFAJARDO@jhmi.edu

8. PERFORMING ORGANIZATION REPORT NUMBER

9. SPONSORING / MONITORING AGENCY NAME(S) AND ADDRESS(ES)
U.S. Army Medical Research and Materiel Command
Fort Detrick, Maryland 21702-5012

10. SPONSORING / MONITORING AGENCY REPORT NUMBER

11. SUPPLEMENTARY NOTES
Report Contains Color

12a. DISTRIBUTION / AVAILABILITY STATEMENT
Approved for Public Release; Distribution Unlimited

12b. DISTRIBUTION CODE

13. ABSTRACT *(Maximum 200 Words)*

14. SUBJECT TERMS
digital mammography, breast cancer, automatic exposure device

15. NUMBER OF PAGES
32

16. PRICE CODE

17. SECURITY CLASSIFICATION OF REPORT	18. SECURITY CLASSIFICATION OF THIS PAGE	19. SECURITY CLASSIFICATION OF ABSTRACT	20. LIMITATION OF ABSTRACT
Unclassified	Unclassified	Unclassified	Unlimited

NSN 7540-01-280-5500

Standard Form 298 (Rev. 2-89)
Prescribed by ANSI Std. Z39-18
298-102

Table of Contents

Introduction

The broad, long-term objective of this IDEA proposal is to achieve optimized image quality for DM within acceptable limits of radiation exposure by developing innovative approaches for controlling DM exposures. These approaches entail using the digital detector and an artificial neural network to control mammographic exposures. This project's specific aims are (1) to use short, low dose pre-exposures of the breast to create "intelligent" regions of interest that determine the exposure parameters for the fully exposed image; and (2) to use an artificial neural network to select exposure parameters (mAs, kVp, and beam filtration) based on "intelligent decisions" that optimize signal-to-noise (SNR) as a function of mean glandular dose.

Body: Progress on Research Tasks & Key Research Accomplishments

Task 1. Determine optimal pixel binning factor and size of exposure-controlling ROI.

The ideal exposure-controlling ROI (ECROI) is large enough so that small, high-density structures such as calcifications are not selected to determine exposure parameters, but small enough so that the image is not smoothed excessively. To determine an optimal ECROI size, we surveyed FFDM images from our clinical image database, evaluating 3-D surface plots to determine where the "peaks" of low exposure areas are located and the range of the super-pixel values in the peaks. This provided information on the effects of the location and size of the ECROI. We evaluated the effect of the ECROI size on the calculation of the SNR (Figures 1-7). Next, we developed software to analyze selected ROIs (super-pixels) of digitally acquired mammograms. The primary two questions to be addressed by these analysis tools are:

1) Which area of the digitally obtained mammogram contains the area of greatest radiographic attenuation (the ECROI)?
2) What portion of the pixel variance in the ECROI is a result of differential breast attenuation (signal) as opposed to random fluctuations (noise)?

With respect to question 1), the immediate objectives of the software programs are:

a) Evaluate the correlation between the number of regions of interest (ROIs) sampled and the correct identification of the ROI containing the area of greatest radiographic attenuation (the ECROI)

b) Evaluate the correlation between ROI size and correct identification of the ECROI

c) Examine the effect of pixel binning on correct identification of the ECROI

The selection of the pixel binning factor involves tradeoffs between readout speed and information loss. We evaluated binning factors of 8 (to form 320μ x 320μ super-pixels) and 16 (giving 640μ x 640μ super-pixels) using images of the test phantom acquired at low exposures. Three-dimensional pixel-value surface plots were compared to similarly

binned plots made using full exposures (Figures 1-4). The location of areas having low ADU values was the same in the low- and high-exposure plots, indicating that these binning factors did not result in unacceptable image smoothing. We then examined ROIs of 800 x 800 pixels (3200μ X 3200μ pixels) (Figures 5-7) and 1600 x 1600 pixels (64,000μ X 64,000μ super-pixels). For the 3200μ X 3200μ pixel ROI, a 6 x 8 grid of ROIs was established. In our experiments (Figures 5 & 6), the ROI positions were held fixed while their side lengths varied between minimum values of approximately 1.7% of the short dimension of the image, to their maximum value, equal to the center-to-center ROI spacing. Average pixel value in the 48 ROIs (Figure 5) were plotted as a function of ROI side length, in units of binned pixels (Figure 6). We then performed similar experiments for 64K μ X 64K μ ROIs. These data were then utilized for task 2 experiments (below) to calculate the contribution of signal to the total variance of the ECROIs.

Task 2. Identify the contribution of signal to the total variance in the ECROI.

This entails distinguishing between contributions to the variance within the ECROI from breast structure and from noise (e.g., x-ray quantum noise or $\sigma_{quantum}$, and additive/system noise or σ_e) in the pre-exposure images. We have used two pre-exposures to permit pixel fluctuations arising from the signal relating to breast structure to be distinguished from those arising from noise. The ECROI is determined from the first pre-exposure. Only detector modules containing the ECROI are read out on the second pre-exposure. Pre-exposure times and initial kVp are scaled according to compressed breast thickness (≥6.5 cm:30 kVp; 6 cm:29 kVp; 5.5 cm:28 kVp; 5 cm:27 kVp; 4.5 cm:26 kVp; ≤4.0 cm:25 kVp). Initial choices for pre-exposure times and kVp are based on values calculated to result in a MGD of approximately 150 mrads to a 50% fat / 50% fibroglandular breast in an exposure time of approximately 1 sec.

Criteria for optimization of tube voltage and external filtration in digital mammography differ from those used in screen-film mammography. This is because the separation of the processes of acquisition and display in the former permits contrast of individual structures to be adjusted when the image is displayed. It is therefore possible to detect objects with low subject contrast provided that the image signal to noise ratio (SNR) is adequate. Thus, rather than maximization of contrast within the constraints of acceptable film darkening and patient dose, beam optimization in digital mammography requires maximization of the image SNR, constrained by acceptable patient dose.

To identify optimum technique factors, the following figure of merit was used:

$$FOM = (SNR)^2/MGD,$$

Where MGD is mean dose to the glandular portion of the breast, and the SNR is Rose's suggested minimum value of 5 [1].

Using simple phantoms with known signals (disks, holes, etc.) that result in signal-induced variances that are easily determined, we calculated the ECROI SNR. Breast tissue equivalent material corresponding to 3 different fat/glandular ratios was used to simulate a range of breast thicknesses and densities. Look-up tables were generated with starting pre-exposure time and kVp for varying breast composition/thickness (288 test conditions) as input data. These data were further refined in task 3 experiments using

anthropomorphic breast phantoms that more closely approximate the spectral content of human breast tissue (see below).

Task 3. Determine how breast structure relates to measured variances. We selected a broad range of breast thickness and radiodensity from our Digital mammography patient image database to empirically determine the contribution to the total variance that arises from breast structure (signal). In order to obtain the best possible estimate of the variance associated with normal breast parenchyma, we selected ROIs from sub-areas of mammograms with obviously high SNR. In those ROIs, the average pixel value and system gain was used to calculate the x-ray quantum variance, $\sigma^2_{quantum}$. Using the measured system noise, σ_e, the contribution to the total variance, σ^2_{total}, from breast tissue was calculated from:.

$$\sigma^2_{signal} = \sigma^2_{total} - \sigma^2_{quantum} - \sigma^2_e$$

After the 2 pre-pulses, we calculated σ^2_{noise} and σ^2_{signal} and used the empirically determined relationship between σ^2_{signal} and $I_{max} - I_{min}$ to infer the magnitude of the signal. The ratio of the inferred signal to σ_{noise} is the SNR following the pre-exposure. This was then used to select exposure parameters for the full exposure. If only the exposure *time* is to be selected (phototiming mode), this is straightforward since $I_{max} - I_{min}$ is directly proportional to mAs and since the quantum noise, σ_q, increases as the square root of the exposure time. In the CCD-based TREX system, the system noise (σ_e) increases as the square root of the exposure time because of the accumulation of thermal electrons in the CCD pixels. This noise was previously characterized over a large range of exposure times.

Results of Phantom Experiments Performed for Tasks 2 & 3:
Following are example plots of measured signal, SNR, and the FOM, as a function of kVp, for a 70/30 fibroglandular/fat equivalent phantom composition, using the signal from the microcalcification-equivalent material. These data were obtained from the DM system at Johns Hopkins. The results of these studies were presented at the 5th International Workshop on Digital Mammography, Toronto, CA, June 11-14, 2000.

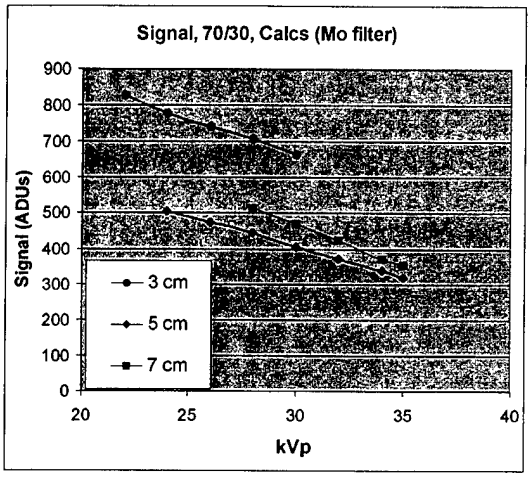

Figure 1

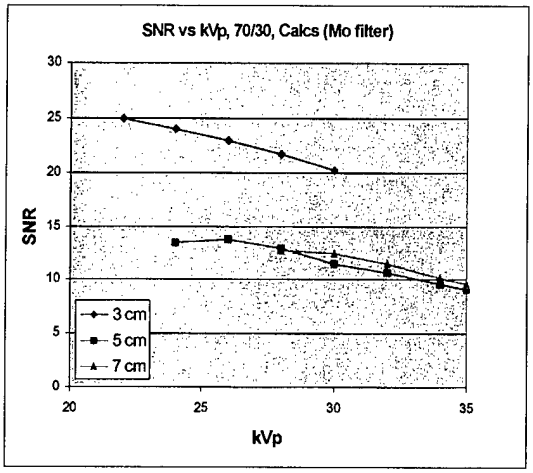

Figure 2

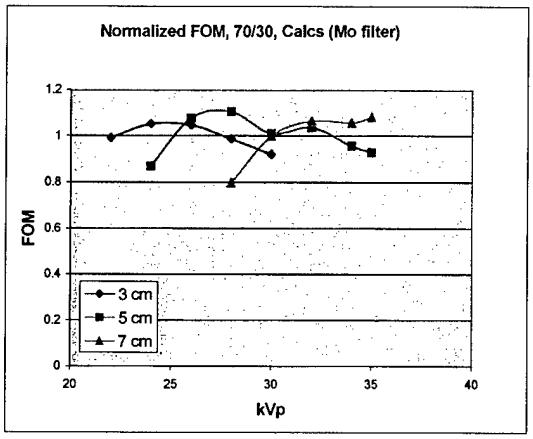

Figure 3

Nine different phantoms were assembled to simulate breasts of three different thicknesses (3 cm, 5 cm, and 7 cm), and three different attenuation equivalent adipose/fibroglandular mass ratios (30/70, 50/50, and 70/30). All blocks of a given phantom had the same adipose /fibroglandular ratio, except for two 5 mm thick blocks, common to all phantoms, that are 100% adipose equivalent. These blocks were placed at the top and bottom of the stack to simulate skin (see figure 4). In each phantom stack assembled, the centrally located block in the stack (the signal block) contained a series of test objects. For the data reported here, the test objects of interest were two stepwedges, one each of calcification equivalent and mass equivalent material. The mass equivalent stepwedge has the same x-ray attenuation as 100% glandular equivalent material, and the microcalcification equivalent step wedge is composed of calcium carbonate. Figure 5 is a schematic of a signal block showing the dimensions of the block and step wedges (other test objects present in the signal block have been omitted for clarity). The thickness of all signal blocks is 2 cm. Images were obtained in manual mode with the phantoms positioned at

the chest wall edge of the receptor, centered left to right. Exposure time was selected to give approximately the same average pixel value in the phantom background area for each phantom/technique combination. For each combination two images were obtained with identical exposure times for the purpose of image subtraction, taking care not to move the phantom between the two exposures. At each site, entrance exposures (mR/mAs) and half value layers (HVLs) were measured for each target/filter/kVp combination used.

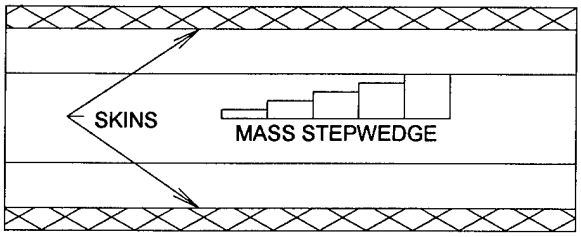

Figure 4: Side view of a 5 cm thick phantom, comprised of one 2 cm thick signal block, two 1 cm thick blank blocks, and two 0.5 cm thick skins.

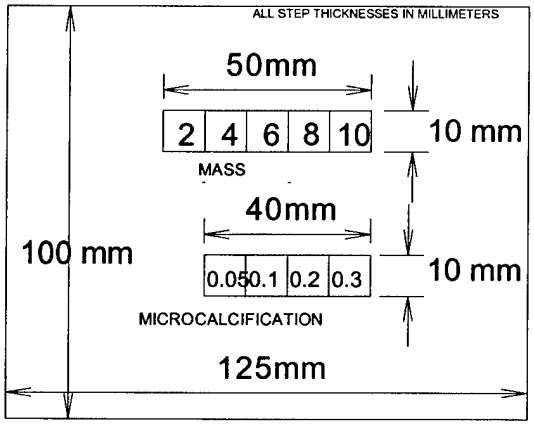

Figure 5: Schematic diagram of a signal block

ECROI Analysis:

Signal was defined as the difference between the average pixel values in a region of interest (ROI) centered on an individual step (but not including the step boundaries), and an equal sized ROI located immediately adjacent to the step, but containing only background. To quantify the image noise, the two images of a given phantom, obtained at a common technique, were subtracted. Image subtraction was performed to remove fixed pattern noise associated with phantom defects, detector non-uniformity, and the heel effect. Noise in a single image was defined as the rms pixel-to-pixel fluctuations in an ROI of 1109 x 511 pixels in the difference image, divided by the square root of two.

Evaluation of acceptable mean glandular dose:
The MGD for each phantom was calculated using its known thickness and composition, and the measured HVL and mR/mAs values from each DM system. For Mo/Mo and Mo/Rh spectra, the parameterized dose tables of Sobol and Wu were utilized to obtain the glandular dose per unit exposure [2]. For the W/Al spectra, normalized (to entrance exposure) MGD values were obtained from the data of Stanton et al. [3]. Their data were extrapolated to 3 cm breast thickness, and interpolation between their published HVL curves was used to obtain correction factors for the particular glandular volume fractions (0.22, 0.40, and 0.61, corresponding to glandular mass fractions of 0.30, 0.50, and 0.70, respectively) used in our study. For the W/Rh spectra, the calculations of Boone were utilized, interpolating between his published HVL and adipose/fibroglandular composition values [4]. All FOM values were obtained by dividing the square of the SNR by the MGD, expressed in units of 10^{-5} Gy (1 mrad).

The measured HVL values for the seven specific target/filter combinations tested at the three sites, as a function of kVp, are shown in Figure 3. Figure 4 shows the corresponding normalized MGD, D_{gN}, calculated for each of the seven spectra, plotted versus the measured HVL. Similarly, Figure 8 shows D_{gN} for each target/filter combination tested, plotted versus kVp. The general tradeoff between loss of contrast and reduction in MGD with increasing kVp is illustrated in Figure 9. In this example, the measured contrast of the 0.3 mm thick (thickest) calcification step in shown for the 5 cm thick, 50/50 phantom.

SNR versus kVp, and the corresponding FOM values vs. kVp have been determined. Figures 10 and 11 show the results obtained for the 300 micron thick step of the calcification stepwedge in the three 50/50 composition phantoms. To illustrate the applicability of these data to objects, the dependence of the FOM on the step thickness for both types of stepwedges is presented in Figures 12 and 13. These data are from images obtained using a Mo/Mo target/filter combination to image a 5 cm thick, 50/50 composition phantom. Finally, Figures 14-16 illustrate the effect on the FOM of changing breast composition, holding breast thickness fixed. Signals were calculated using the 10 mm thick mass equivalent step.

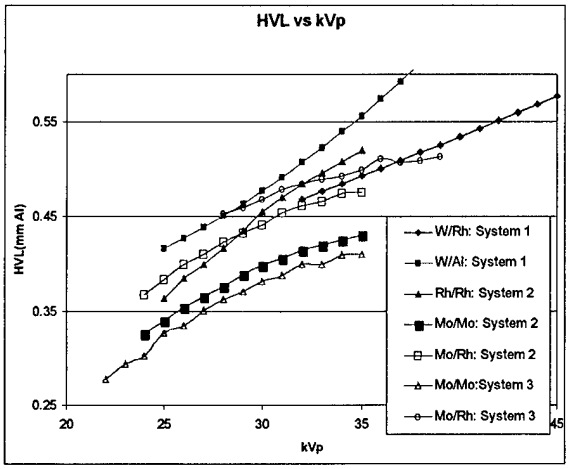

Figure 6: Measured HVLs , plotted versus

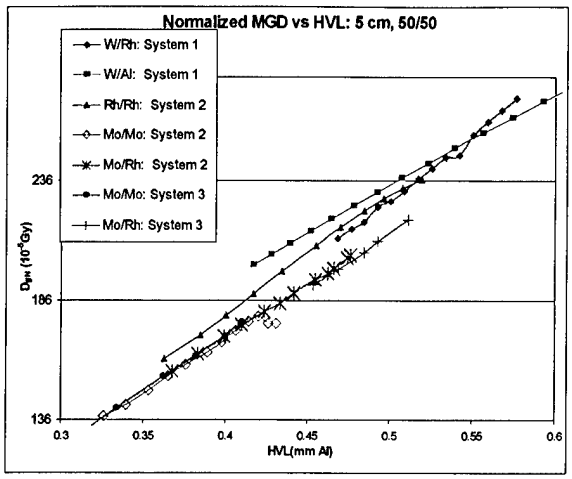

Figure 7: Normalized mean glandular dose versus HVL, assuming a 5 cm thick, 50/50phantom

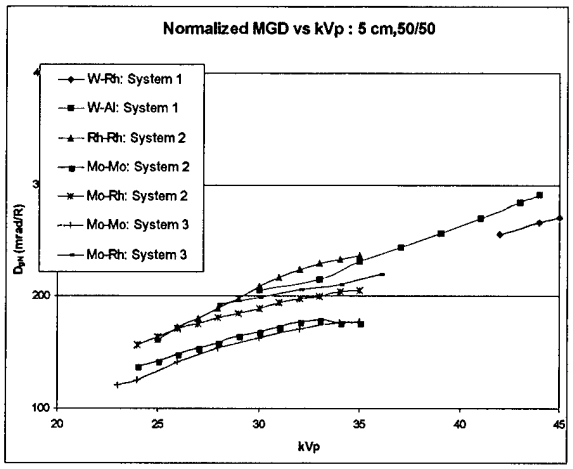

Figure 8: Normalized mean glandular dose vs. kVp assuming a 5 cm thick, 50/50 phantom

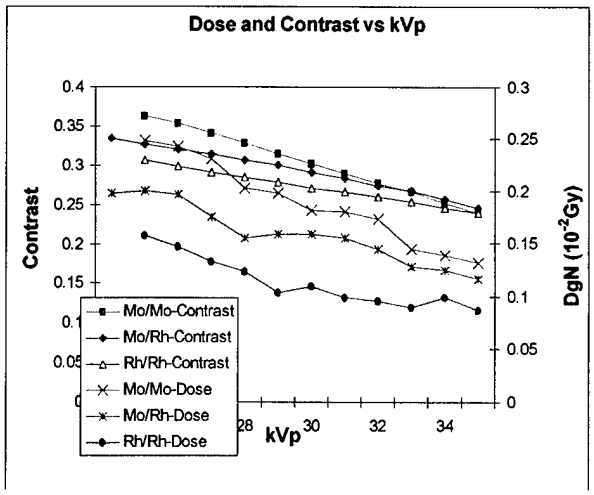

Figure 9: Dose and contrast versus kVp using the 0.3 mm calcification step in a 5 cm thick, 50/50 phantom

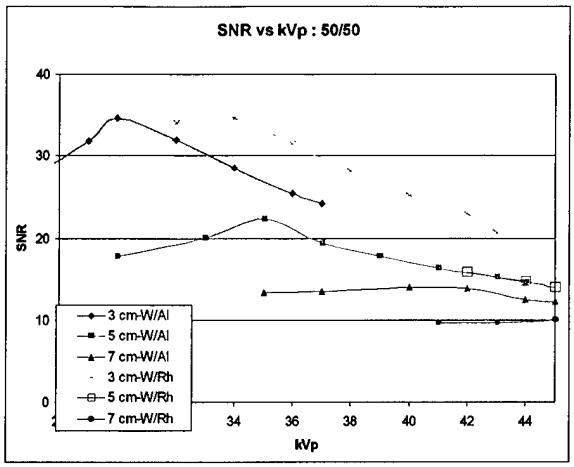

Figure 10: SNR vs. kVp.

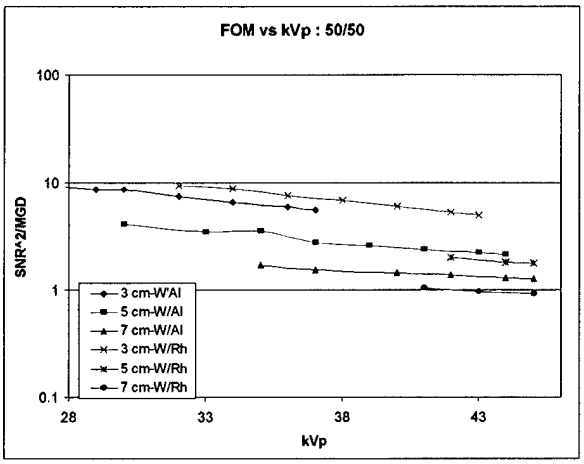

Figure 11: FOM vs. kVp.

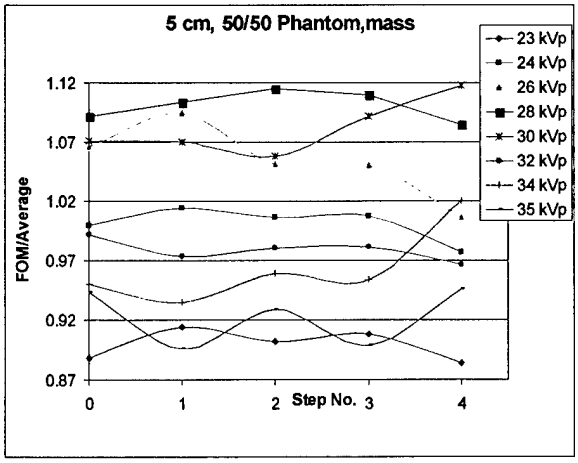

Figure 12: FOM values for the five steps of the mass stepwedge, normalized by the average value for each step. The average FOM values ranged from 0.2 (step 0) to 0.011(step 4). Imaging data from the 5 cm 50/50 phantom.

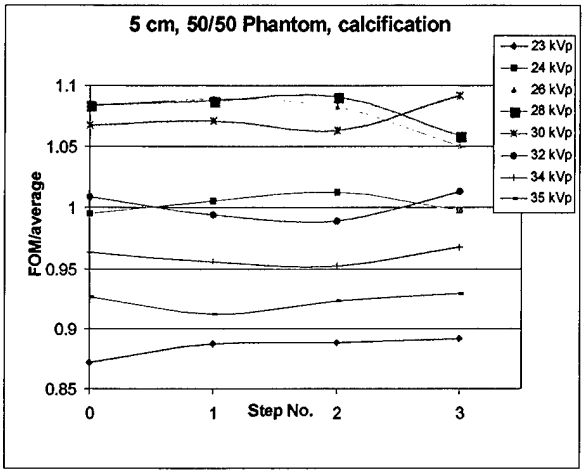

Figure 13: FOM values for the four steps of the calcification stepwedge, normalized by the average value for each step. The average FOM values ranged from 1.4 (step 0) to 0.64 (step 3). Data are imaging the 5 cm 50/50 phantom.

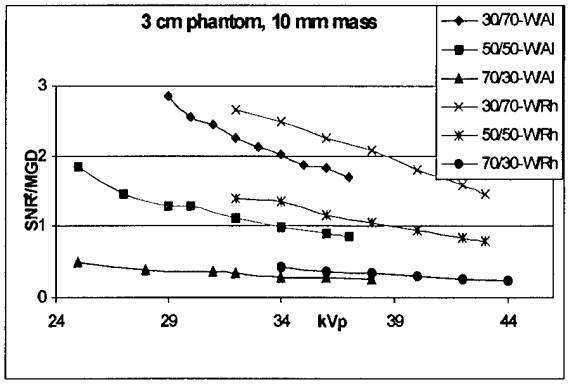

Figure 14: FOM vs kVp for 3 cm thick phantoms of three compositions.

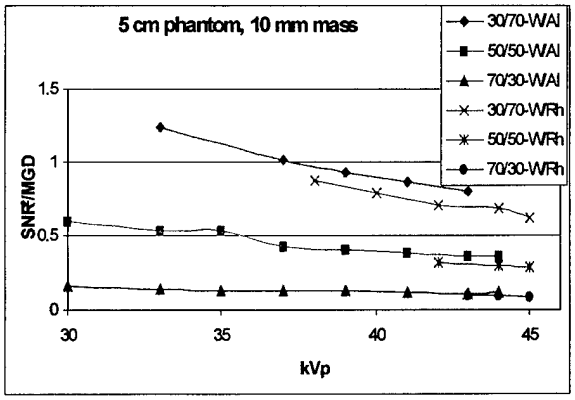

Figure 15: FOM vs kVp for 5 cm thick phantoms of three compositions

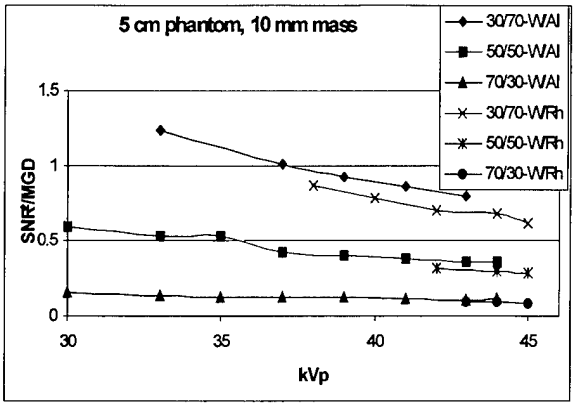

Figure 16: FOM vs kVp for 7 cm thick phantoms of three compositions.

Task 4. Optimize mAs, kVp, and Filter Selection Based on the Results of the Pre-exposures.

Optimization is based on maximization of the figure of merit: FOM=(SNR^2/MGD). We have used the added information provided by the spatially varying signal levels in the pre-exposure ROIs to calculate a more refined estimate of the MGD than is possible using simply compressed thickness. To do this, the mean pixel value in each ROI is used to determine the relative transmission through the breast at that location. In regions of uniform thickness (all regions whose entrance surface is in direct contact with the compression paddle), variations in x-ray transmission are due to variations in breast composition. The region of the breast above each ROI is assumed to consist of two skin and subcutaneous layers with a uniform mixture of adipose and fibro-glandular tissue in between. The x-ray transmission through each region determines an adipose/ fibroglandular composition ratio. Thus, for a given kVp, filter, and mAs, the MGD for the region of the breast above each ROI can be calculated separately, and the result summed to obtain an average MGD.

Preliminary Results: Task 4:

Software has been developed for analysis of digitally acquired mammograms. The primary two questions to be addressed by these analysis tools may be generalized as follows:

1) Which area of the digitally obtained mammogram contains the area of greatest radiographic attenuation (the ECROI)?
2) What portion of the pixel variance in the ECROI is a result of differential breast attenuation (signal) as opposed to random fluctuations (noise)?

With respect to question 1), the immediate objectives of these programs are:

1) Evaluate the correlation between the number of regions of interest (ROIs) sampled and the correct identification of the ROI containing the area of greatest radiographic attenuation (the ECROI)
2) Evaluate the correlation between ROI size and correct identification of the ECROI

3) Examine the effect of pixel binning on correct identification of the ECROI

Figure 17 below shows an example of a digitally obtained mammogram in which a 6 x 8 grid of ROIs has been established. The figure shows the mammogram, labeled with numbers whose locations correspond to the centers of the ROIs.

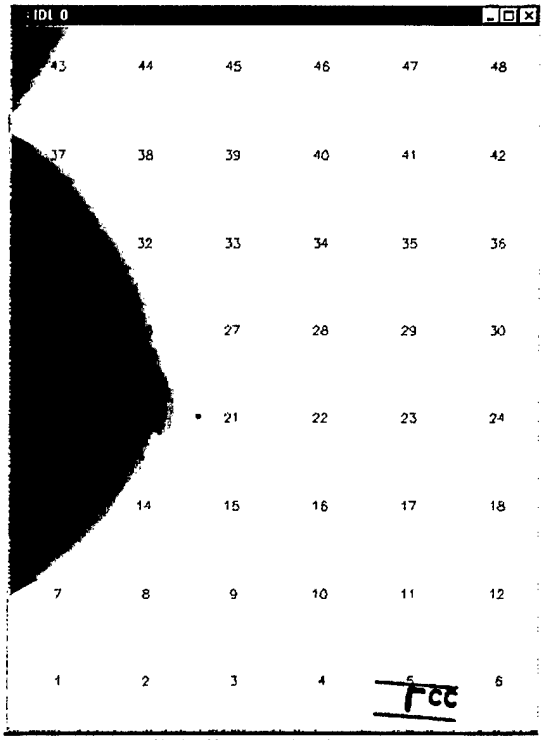

Figure 17: A digitally acquired mammogram, annotated with the locations of a 6 x 8 square grid of ROIs. The numerals are located at the centers of the square ROIs. The ROI positions are held fixed, while their side lengths are varied between minimum values of approximately 1.7% of the short dimension of the image, to their maximum value, equal to the center-to-center ROI spacing.

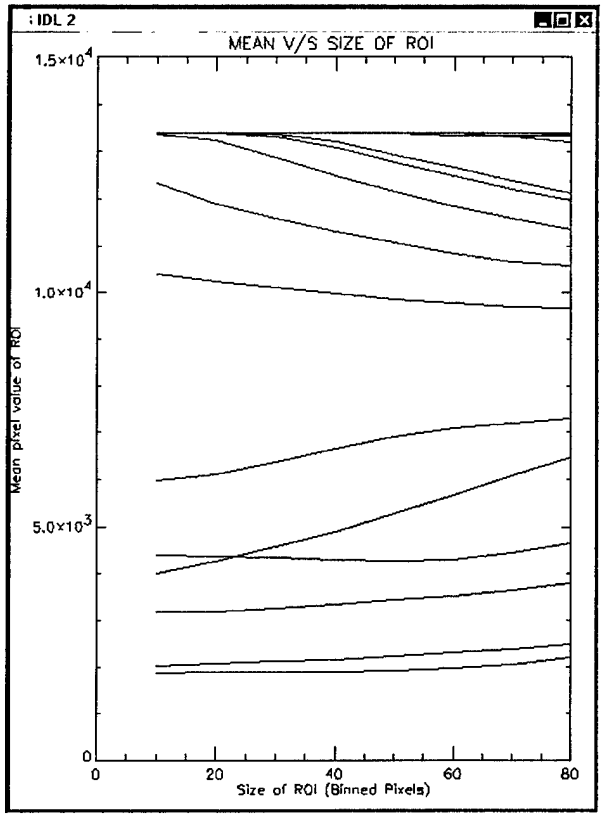

Figure 18: Average pixel value in the 48 ROIs of Figure 1, plotted as a function of ROI side length, in units of binned pixels. For the example shown, the ECROI (that with the lowest average pixel value) is the same for all ROI sizes tested. Its center is at the position labeled '19' in Figure 17. ROIs whose average pixel value is always large and constant (top of the graph) are located outside the region of the breast.

Figure 18 is a plot of the mean values of each ROI, plotted as a function of ROI size. The ROI with the lowest value is the ECROI. For the example shown, the ECROI is ROI #19. The contour plot of the pixel values, shown below in Figure 19, verifies that this is in fact the most highly attenuating portion of the breast.

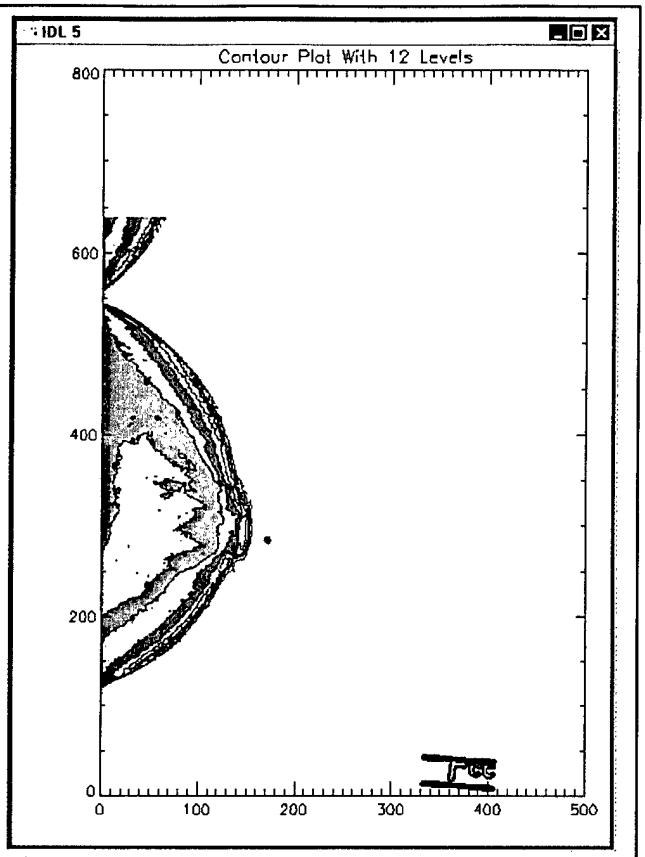

Figure 19: Contour plot of the pixel values in the digital mammogram of Figure 1.

Progress Since Last Report

We have developed analysis tools to evaluate the effect of radiographic heterogeneity on the selection of the ECROI and have performed analysis of digital mammograms of patients with a variety of compositions and breast sizes. Table 1 below provides the calculated ratios of root mean square signal to root mean noise for 20 digital mammographic images evaluated in 5 patients with a variety of breast compositions (radiodensity). For each study, the compressed breast thickness was 4 -5 cm and a 28 kVp Mo/Mo beam was used. The third column gives the total variance in the ECROI. The fifth column gives the portion of the variance that is due to noise, as determined by uniform irradiation studies. The last column gives the ratio of the RMS signal to the RMS noise. These ratios suggest the approximate magnitude of the target SNR values to be used in the AEC algorithm.

TABLE 1: Ratio of RMS Signal to RMS Noise

	Average	Total Variance	mAs	Noise Variance	Signal Variance	SNR
Patient 1	1422	17986	43	745	17242	4.8
	1420	11556	43	744	10812	3.8
	1504	29009	46	780	28229	6.0
	1630	23148	50	835	22313	5.2
Patient 2	2031	36416	62	1019	35397	5.9
	1964	16243	60	987	15255	3.9
	1964	25290	60	987	24303	5.0
	1972	26219	60	991	25228	5.0
Patient 3	1535	9923	47	794	9129	3.4
	1430	16615	44	748	15867	4.6
	1458	14053	44	760	13293	4.2
	1461	19624	45	762	18863	5.0
Patient 4	1577	25117	48	812	24305	5.5
	1502	20446	46	779	19667	5.0
	1547	22630	47	799	21831	5.2
	1311	35793	40	698	35095	7.1
Patient 5	2204	49051	67	1102	47949	6.6
	1727	20817	53	879	19938	4.8
	2041	22180	62	1024	21156	4.5
	2329	39980	71	1163	38816	5.8

Table 2. Log mAs versus Average ADU, Variance and Log (Sigma)

		Bright 1			Bright 2			Dark 1		Dark 2	
mAs	log(mAs)	Average ADU	Variance	log(sigma)	Average ADU	Variance	log(sigma)	Average ADU	Variance	Average ADU	Variance
3	0.5	75	167	1.1	76	195	1.1	7.7	52	7.0	40
6	0.8	175	215	1.2	176	215	1.2	7.0	41	7.1	42
10	1.0	311	279	1.2	310	280	1.2	6.9	39	6.9	40
20	1.3	644	448	1.3	644	448	1.3	6.8	40	6.8	39
40	1.6	1311	803	1.5	1310	808	1.5	7.0	41	7.2	44
80	1.9	2637	1507	1.6	2636	1504	1.6	7.1	44	7.1	46
160	2.2	5306	2979	1.7	5306	2980	1.7	7.4	58	7.1	53
240	2.4	7984	4734	1.8	7981	4742	1.8	7.6	72	7.5	71
325	2.5	10832	8617	2.0	10852	7597	1.9	7.9	94	8.0	94
400	2.6	13376	11067	2.0	13377	11054	2.0	8.3	118	8.0	115

Figure 20a. Average ADU vs. mAs Linearity as a Function of X-ray Exposure

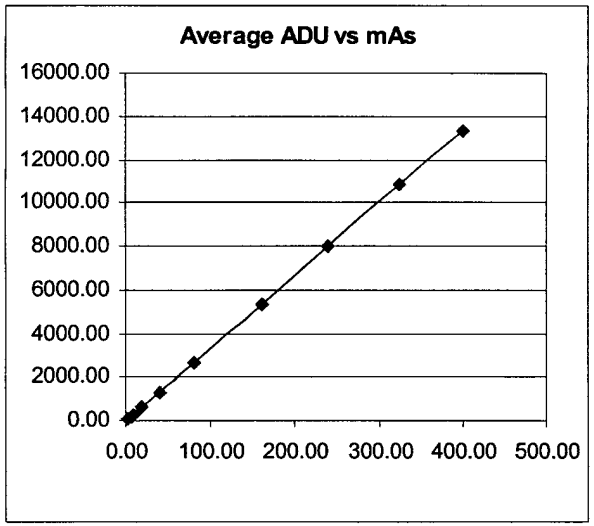

Figure 20b. log(sigma) vs log(mAs) Log of the SD vs. log of the mAs

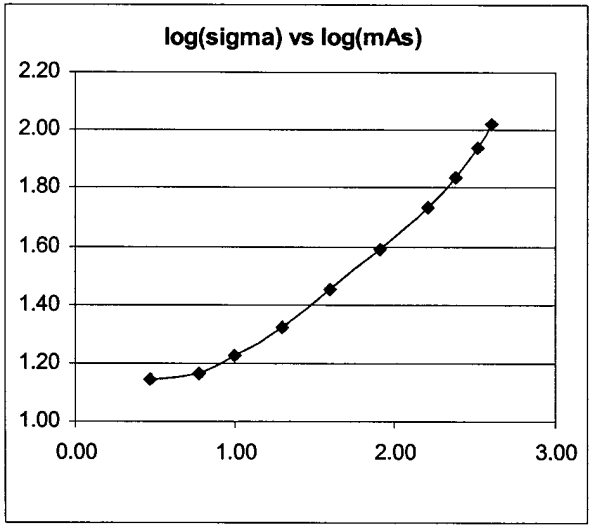

Figure 20c. Variance vs. Average ADU

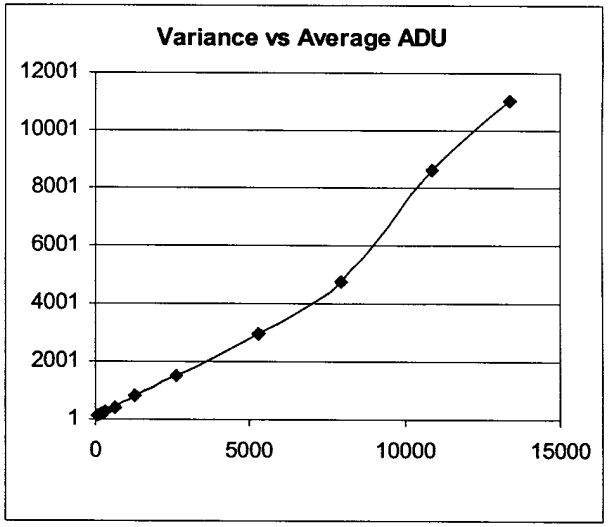

We have carefully evaluated linearity as a function of x-ray exposure (Table 2 & Figure 20a) with phantom experiments using a 4cm acrylic phantom imaged at 28 kVp. The quantum limited range of operation was determined from a log-log plot of the pixel variance vs the mAs (Figure 20b). As is shown, the linear region between ~ 1.0 and 2.5 on the horizontal axis (Figure 20b) indicated quantum limited operation. Below log(mAs) = 1.0, the system noise constitutes a significant part of the total noise, and above log(mAs) = 2.5, there is a slight departure from quantum limited operation, probably due to imperfectly corrected fixed pattern noise at these high exposure levels. This departure can also be seen in the two data points in the upper right portion of Figure 20c. We will use the quantum limited region in our calculation of the final mAs, based on the measured signal variance (pixel variance due to differential breast attenuation) in the ECROI following pre-exposure. .

We have also developed analysis programs for determination of the pixel variance due to differential breast attenuation (signal variance), and are characterizing intrinsic detector noise. Table 3 below provides data on the total variance in the ECROI, including its components due to signal and noise.

Table 3. Total Variance in the ECROI as a function of the Signal and Noise Components

mAs	Average	Total Variance	Noise Variance	Signal Var	sqrt(sig var)
3	43	262	167	95	10
6	94	409	215	194	14
10	166	700	279	421	21
20	343	2110	448	1662	41
40	698	7548	803	6745	82
80	1401	29174	1507	27667	166
160	2813	116440	2979	113461	337
240	4224	261613	4734	256879	507
325	5724	481110	8617	472493	687
400	7056	732557	11067	721490	849

FIGURE 21a. Average Pixel Value in ECROI

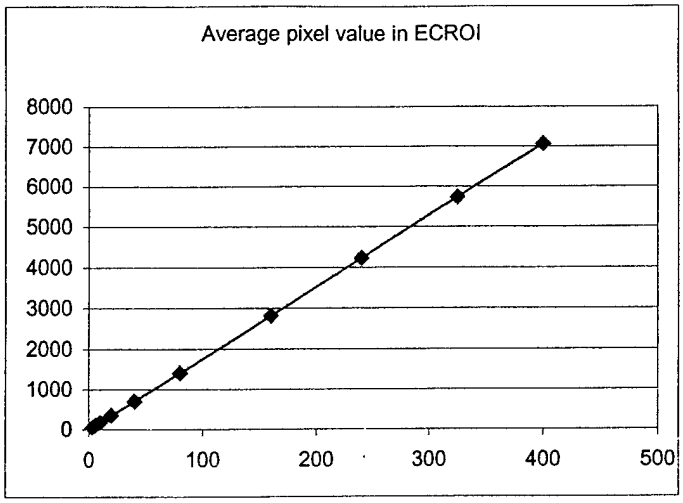

Figure 21b. Total Variance in ECROI

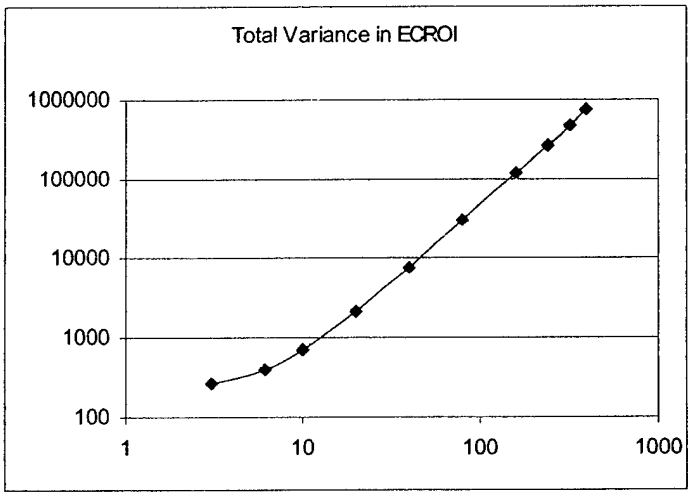

Figure 21c. S.D. in ECROI due to Signal only

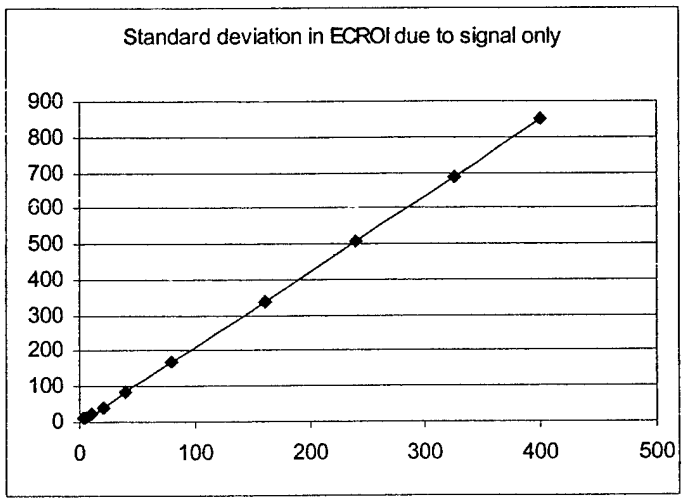

These results demonstrate that the total variance in the ECROI is the arithmetic sum of the signal and noise variances. As shown in Figure 21c, the signal variance is proportional to the square of the mAs, as would be expected for a linear system. Therefore, determination of the total variance at any given mAs, along with the known noise variance at that mAs, permits calculation of the SNR for all mAs values. In the context of AEC development, this means that we can quickly assess the RMS signal variance in the ECROI following pre-exposure at low mAs, and extrapolate to the target mAs value that will result in the desired SNR.

Reportable Outcomes:

Abstracts & Presentations:

The 1999 Radiological Society of North America, Chicago, IL, November 27- December 3, 1999: "Development of a quality control system for full-field digital mammography". MJ Yaffe, MB Williams, LT Niklason, GE Mawdsley, AD Maidment, Radiology 209(P) (1999) 160.

The 5th International Workshop on Digital Mammography, Toronto, CA, June 11-14, 2000: "Beam Optimization for Digital Mammography". MB Williams, M More, V Venkatakrishnan, L Niklason, MJ Yaffe, G Mawdsley, A Bloomquist, A Maidment, D Chakraborty, C Kimme-Smith, LL Fajardo.

Publication:

Williams MB, Mangiafico PA, Simoni PU. Noise power spectra of images from digital mammography detectors. Med Phys 2000:6(7);1279-1293.

Conclusions:

The analysis of SNR and FOM as a function of kVp, shown in Figures 10 and 11, indicates that although the image SNR tends to decrease monotonically for all systems with increasing kVp, the accompanying MGD reduction results in fairly flat FOM curves. This is primarily due to tube loading, since it was not possible to obtain the same exit exposure at all kVps (that is, the tube output was insufficient to compensate for the lower transmission through the phantoms). Thus the falling SNR (and the falling MGD) with decreasing kVp are really consequences of falling exposure.

For a given phantom/technique combination, the SNR, and thus the *magnitude* of the FOM, increases with increasing step thickness for both types of stepwedge. However, the *shape* of the FOM vs. kVp curves for a given target/filter/phantom combination are essentially independent of step thickness, and are similar for mass and calcification equivalent signals. This is illustrated by the example shown in Figures 12 and 13. This implies that the result of the optimization is not sensitively dependent on signal amplitude.

Figures 14-16 illustrate a clear advantage to using rhodium filtration for thin breasts, but that for breasts 5 cm or thicker, aluminum filtration becomes increasingly advantageous. Similar statements can be made for the molybdenum target systems tested, where molybdenum filtration was superior for 3 cm phantoms of all compositions, but rhodium filtration produced better results for 5 and 7 cm thick phantoms of all compositions. These data suggest that the choice of external filtration is potentially more significant in determination of the overall FOM of a DM system than is choice of tube voltage.

Fahrig and Yaffe developed a model for optimizing spectral shape in digital mammography, and used it to calculate kVp values producing maximum SNR at a fixed dose for W and Mo spectra [5]. They found that, for a fixed MGD of 0.6 mGy (60 mrads), the peak SNR occurred in the 24-31 kVp range (W spectrum) and 25-29 kVp range (Mo spectrum) for 4 – 8 cm breast thickness, and 50/50 breast composition. Their results were the same, whether the lesion type modeled was infiltrating ductal carcinoma or microcalcification.

Jennings et al. used a computational approach to identify maximum FOM values (FOM = SNR^2/MGD) for a variety of target/filter combinations, and breast thicknesses [6]. They found that for a Mo/Mo beam used to image 3-6 cm, 50/50 breasts, the FOM peaks at 27-28 kVp, and changes slowly with changing kVp near the peak values. Very similar FOM vs. kVp curves were obtained for Mo/Mo, Mo/Rh, and W/Al spectra, applied to 6 cm thick, 50/50 composition breasts. The general trends in our data appear to be consistent with those of these previous studies.

Our results using the Lorad CCD-based detector demonstrate that the total variance in the ECROI is the arithmetic sum of the signal and noise variances, and that knowledge of detector noise characteristics for a given attenuating thickness and kVp, permits the RMS variance due to differential breast attenuation to be obtained. Because the system is linear with respect to x-ray fluence, the signal variance is proportional to the square of the mAs. Therefore, calculation of both the signal and noise variance at any given mAs is possible, enabling permitting calculation of the SNR as a function of mAs .

Implementation of the first generation of automatic exposure control device on the digital mammography system results in images having satisfactory image quality, SNR and mean glandular dose. For 16 patients undergoing both conventional mammography and digital mammography, the implemented AEC for the digital system performed satisfactorily. We now have nearly complete data to finalize the algorithms for a functional AEC device for the experimental digital mammography system.

References

1. Rose A. Vision: Human and Electronic. Plenum Press, New York, N.Y., 1973.

2. Sobol WT and Wu, X. Parameterization of mammography normalized average glandular dose tables. Medical Physics 24(4), 547-555. 1997.

3. Stanton L., Villafana, T., Day, J., and Lightfoot, D. (1984). Dosage evaluation in mammography. Radiology 150, 577-584.

4. Boone, J. (1999). Glandular breast dose for monoenergetic and high-energy x-ray beams: Monte Carlo assessment. Radiology 213, 23-37.

5. Fahrig, R. and Yaffe, M. (1994). Optimization of spectral shape in digital mammography: Dependence on anode material, breast thickness, and lesion type. Med.Phys. 21, 1473-1481.

6. Jennings, R.L., Quinn, P.W., Gagne, R.M., and Fewell, T.R. (1993). Evaluation of x-ray sources for mammography. Proc SPIE 1896, 259-268.

Appendix

Publication Reprint

BEAM OPTIMIZATION FOR DIGITAL MAMMOGRAPHY

Mark B. Williams[*], Mitali More[*], Vaidehi Venkatakrishnan[%], Loren Niklason[^], Martin J. Yaffe[#], Gordon Mawdsley[#], Aili Bloomquist[#], Andrew Maidment[**], Dev Chakraborty[^^], Carolyn Kimme-Smith[##], and Laurie L. Fajardo[***]

* University of Virginia, [%]Beth Israel Hospital, ^General Electric Medical, [#]University of Toronto, **Thomas Jefferson University, ^^University of Pennsylvania, [##]UCLA, [***]Johns Hopkins University

Table of Contents

1.0 Introduction

Criteria for optimization of tube voltage and external filtration in digital mammography (DM) differ from those used in screen-film mammography. This is because the separation of the processes of acquisition and display in the former permits the contrast of individual structures to be adjusted when the image is viewed. It is therefore possible to detect objects with low subject contrast provided that the image signal to noise ratio (SNR) is adequate. Thus, rather than maximization of contrast within the constraint of acceptable film darkening and patient dose, beam optimization in digital mammography requires maximization of the image SNR, constrained by acceptable patient dose.

The goal of this study is to identify, for each of several currently available DM systems, technique factors that result in the highest SNR per unit radiation dose, and to do so for a range of breast thickness and adipose/fibroglandular ratio. Data from three different early commercial DM systems, located at three different university test sites, are presented here. Each of these sites is participating in a coordinated clinical evaluation of the DM systems, and a major purpose of our study is to provide guidelines for technique factors to be used during the clinical evaluation.

To identify optimum technique factors, we have chosen the following figure of merit (FOM),

$$FOM = (SNR)^2/MGD,$$

where MGD is the mean dose to the glandular portion of the breast, and the SNR is as defined in section 2.2 below. This FOM is independent of exposure (in the x-ray quantum-limited regime of operation), and has been used previously by others in mammographic beam optimization studies (Jennings et al., 1993; Boone et al., 1990).

2.0 Materials and Methods

2.1 Data Acquisition

Three DM units from three different manufacturers were used in the study. The units from Fischer, GE, and Trex will hereafter be referred to as Systems 1, 2, and 3, respectively. A common set of phantoms was circulated between the physicists participating in the study. The phantoms were assembled from stacks of blocks of breast equivalent material (CIRS, Inc., Norfolk, VA). Nine different phantoms were assembled and imaged, simulating breasts of three different thicknesses (3 cm, 5 cm, and 7 cm), and three different attenuation equivalent adipose/fibroglandular mass ratios (30/70, 50/50, and 70/30). All blocks of a given phantom had the same adipose/fibroglandular ratio, except for two 5 mm thick blocks, common to all phantoms, that are 100% adipose equivalent. These blocks were placed at the top and bottom of the stack to simulate skin (see figure 1). In each phantom stack assembled, the centrally located block in the stack (the signal block) contained a series of test objects. For the data reported here, the test objects of interest were two stepwedges, one each of calcification equivalent and mass equivalent material. The mass equivalent stepwedge has the same x-ray attenuation as 100% glandular equivalent material, and the microcalcification equivalent step wedge is composed of calcium carbonate. Figure 2 is a schematic of a signal block showing the dimensions of the block and step wedges (other test objects present in the signal block have been omitted for clarity). The thickness of all signal blocks is 2 cm. Images were obtained in manual mode with

the phantoms positioned at the chest wall edge of the receptor, centered left to right. Exposure time was selected to give approximately the same average pixel value in the phantom background area for each phantom/technique combination. For each combination two images were obtained with identical exposure times for the purpose of image subtraction, taking care not to move the phantom between the two exposures. At each site, entrance exposures (mR/mAs) and half value layers (HVLs) were measured for each target/filter/kVp combination used.

2.2 Image Analysis

Signal was defined as the difference between the average pixel values in a region of interest (ROI) centered on an individual step (but not including the step boundaries), and an equal sized ROI located immediately adjacent to the step, but containing only background. To quantify the image noise, the two images of a given phantom, obtained at a common technique, were subtracted. Image subtraction was performed to remove fixed pattern noise associated with phantom defects, detector nonuniformity, and the heel effect. Noise in a single image was defined as the rms pixel-to-pixel fluctuations in an ROI of 1109 x 511 pixels in the difference image, divided by the square root of two.

2.3 Calculation of MGD

Table I lists each of the target and filter combinations tested in the study. Also given for each

Table I

Target	**Filter**	**kVp range**	**HVL range (mm Al)**
Molybdenum	Molybdenum	22-35	0.26-0.43
Molybdenum	Rhodium	24-39	0.37-0.51
Rhodium	Rhodium	25-35	0.36-0.52
Tungsten	Aluminum	29-45	0.46-0.77
Tungsten	Rhodium	32-45	0.47-0.58

Target/filter combinations, kVp ranges, and HVL ranges of the systems tested. Two of the three mammographic systems used Mo/Mo and Mo/Rh combinations. In those cases, the kVp and HVL ranges given represent the pooled values from both systems.

target/filter combination are the range of kVps used, and the corresponding HVL range. In several cases, the same target/filter combination was available on more than one DM system. Table I lists the combined kVp and HVL ranges from all systems.

The MGD for each phantom was calculated using its known thickness and composition, and the measured HVL and mR/mAs values from each DM system. For Mo/Mo and Mo/Rh spectra, the parameterized dose tables of Sobol and Wu were utilized to obtain the glandular dose per unit exposure (Sobol and Wu, 1997). For the W/Al spectra, normalized (to entrance exposure) MGD values were obtained from the data of Stanton et al. (Stanton et al., 1984). Their data were extrapolated to 3 cm breast thickness, and interpolation between their published HVL curves was used to obtain correction factors for the particular glandular volume fractions (0.22, 0.40, and 0.61, corresponding to glandular mass fractions of 0.30, 0.50, and 0.70, respectively) used in our study. For the W/Rh spectra, the calculations of Boone were utilized, interpolating between his published HVL and adipose/fibroglandular composition values (Boone, 1999). All FOM values were obtained by dividing the square of the SNR by the MGD, expressed in units of 10^{-5} Gy (1 mrad).

3.0 Results

The measured HVL values for the seven specific target/filter combinations tested at the three sites, as a function of kVp, are shown in Figure 3. Figure 4 shows the corresponding normalized MGD, D_{gN}, calculated for each of the seven spectra, plotted versus the measured HVL. Similarly, Figure 5 shows D_{gN} for each target/filter combination tested, plotted versus kVp. The general tradeoff between loss of contrast and reduction in MGD with increasing kVp is illustrated in Figure 6. In this example, the measured contrast of the 0.3 mm thick (thickest) calcification step in shown for the 5 cm thick, 50/50 phantom.

For each of the three DM systems, SNR versus kVp, and the corresponding FOM values vs. kVp have been determined. Figures 7-12 show the results obtained for the 300 micron thick step of the calcification stepwedge in the three 50/50 composition phantoms, for each of the three

imaging systems. To illustrate the applicability of these data to objects, the dependence of the FOM on the step thickness for both types of stepwedges is presented in Figures 13 and 14. These data are from images obtained on System 3, using a Mo/Mo target/filter combination to image a 5 cm thick, 50/50 composition phantom. Finally, Figures 15-17 illustrate the effect on the FOM of changing breast composition, holding breast thickness fixed. These data were obtained using System 1, and signals were calculated using the 10 mm thick mass equivalent step.

4.0 Discussion and Conclusions

The analysis of SNR and FOM as a function of kVp, shown in Figures 7-12, indicates that although the image SNR tends to decrease monotonically for all systems with increasing kVp, the accompanying MGD reduction results in fairly flat FOM curves. Note, however, in the case of System 1, the SNR falls at low kVp. This is primarily due to tube loading, since it was not possible to obtain the same exit exposure at all kVps (that is, the tube output was insufficient to compensate for the lower transmission through the phantoms). Thus the falling SNR (and the falling MGD) with decreasing kVp are really consequences of falling exposure.

For a given phantom/technique combination, the SNR, and thus the *magnitude* of the FOM, increases with increasing step thickness for both types of stepwedge. However, the *shape* of the FOM vs. kVp curves for a given target/filter/phantom combination are essentially independent of step thickness, and are similar for mass and calcification equivalent signals. This is illustrated by the example shown in figures 13 and 14. This implies that the result of the optimization is not sensitively dependent on signal amplitude.

Figures 15-17 illustrate that, at least in the case of System 1, there is a clear advantage to using rhodium filtration for thin breasts, but that for breasts 5 cm or thicker, aluminum filtration becomes increasingly advantageous. Similar statements can be made for the molybdenum target systems tested, where molybdenum filtration was superior for 3 cm phantoms of all compositions, but rhodium filtration produced better results for 5 and 7 cm thick phantoms of all

compositions. These data suggest that the choice of external filtration is potentially more significant in determination of the overall FOM of a DM system than is choice of tube voltage.

Fahrig and Yaffe developed a model for optimizing spectral shape in digital mammography, and used it to calculate kVp values producing maximum SNR at a fixed dose for W and Mo spectra (Fahrig and Yaffe, 1994). They found that, for a fixed MGD of 0.6 mGy (60 mrads), the peak SNR occurred in the 24-31 kVp range (W spectrum) and 25-29 kVp range (Mo spectrum) for 4 – 8 cm breast thickness, and 50/50 breast composition. Their results were the same, whether the lesion type modeled was infiltrating ductal carcinoma or microcalcification.

Jennings et al. used a computational approach to identify maximum FOM values (FOM = SNR^2/MGD) for a variety of target/filter combinations, and breast thicknesses. They found that for a Mo/Mo beam used to image 3-6 cm, 50/50 breasts, the FOM peaks at 27-28 kVp, and changes slowly with changing kVp near the peak values. Very similar FOM vs. kVp curves were obtained for Mo/Mo, Mo/Rh, and W/Al spectra, applied to 6 cm thick, 50/50 composition breasts. The general trends in our data appear to be consistent with those of these previous studies.

One limitation of our study is that only large area (low frequency) signals were considered. Other test objects in the signal blocks (simulated microcalcifications, for example), may permit some spatial frequency-dependent optimization, but those data have not yet been analyzed. Conversely, noise was calculated from the RMS pixel-to-pixel variations. This is equivalent to estimating the area under the two dimensional noise power spectrum (NPS) out to the Nyquist frequency. Other valid scalar measures of noise, such as the low frequency NPS, would give different results. Finally, this paper does not discuss detector saturation effects, which are important when imaging thick, dense breasts.

Acknowledgements

We would like to thank Mahadevappa Mahesh, Ph.D. at Johns Hopkins University, for his help in getting the data for this study. We also would like to acknowledge the contributions of Piero Simoni, Ph.D. in the development of image analysis software.

References

Boone, J. (1999). Glandular breast dose for monoenergetic and high-energy x-ray beams: Monte Carlo assessment. Radiology *213*, 23-37.

Boone, J., Shaber, G., and Tecotzky, M. (1990). Dual energy mammography: A detector analysis. Med.Phys. *17*, 665-675.

Fahrig, R. and Yaffe, M. (1994). Optimization of spectral shape in digital mammography: Dependence on anode material, breast thickness, and lesion type. Med.Phys. *21*, 1473-1481.

Jennings, R.L., Quinn, P.W., Gagne, R.M., and Fewell, T.R. (1993). Evaluation of x-ray sources for mammography. Proc SPIE *1896*, 259-268.

Sobol, WT and Wu, X. Parameterization of mammography normalized average glandular dose tables. Medical Physics 24(4), 547-555. 1997.

Stanton, L., Villafana, T., Day, J., and Lightfoot, D. (1984). Dosage evaluation in mammography. Radiology *150*, 577-584.

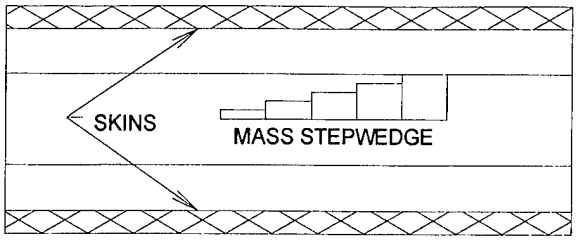

Figure 1: Side view of a 5 cm thick phantom, comprised of one 2 cm thick signal block, two 1 cm thick blank blocks, and two 0.5 cm thick skins.

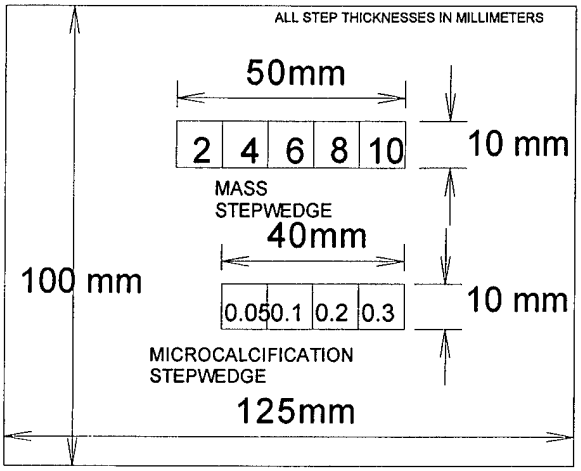

Figure 2: Schematic diagram of a signal block.

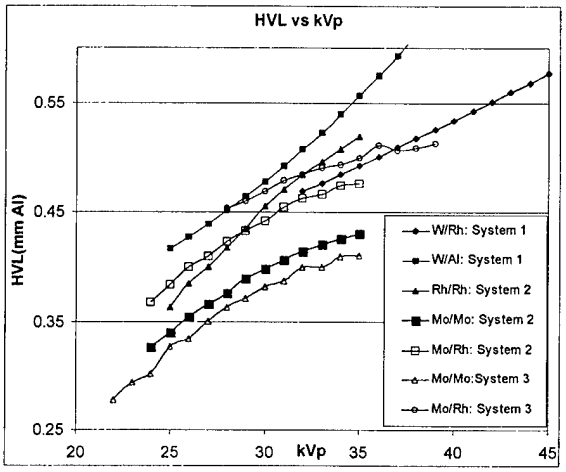

Figure 3: Measured HVLs for the three DM systems, plotted versus kVp.

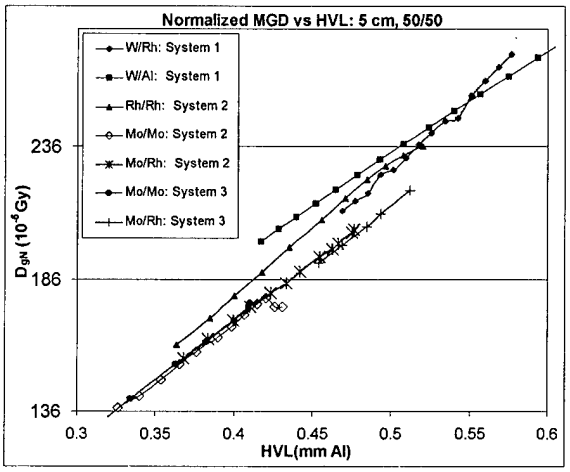

Figure 4: Normalized mean glandular dose versus HVL, for the DM units tested, assuming a 5 cm thick, 50/50 phantom.

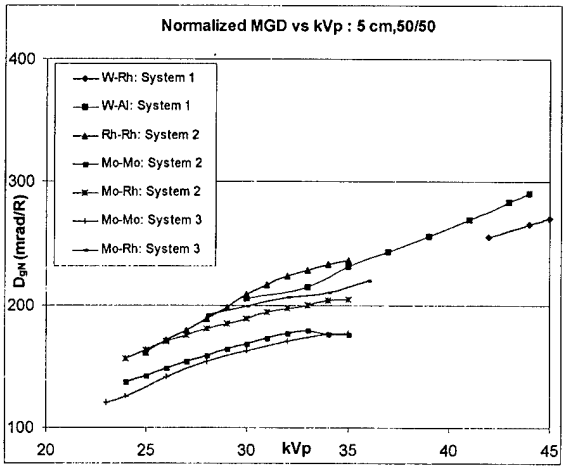

Figure 5: Normalized mean glandular dose vs. kVp for the DM units tested, assuming a 5 cm thick, 50/50 phantom.

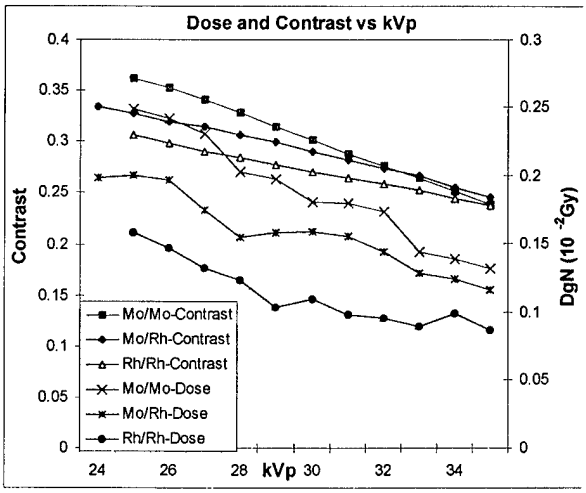

Figure 6: Dose and contrast versus kVp for System 2, using the 0.3 mm calcification step in a 5 cm thick, 50/50 phantom.

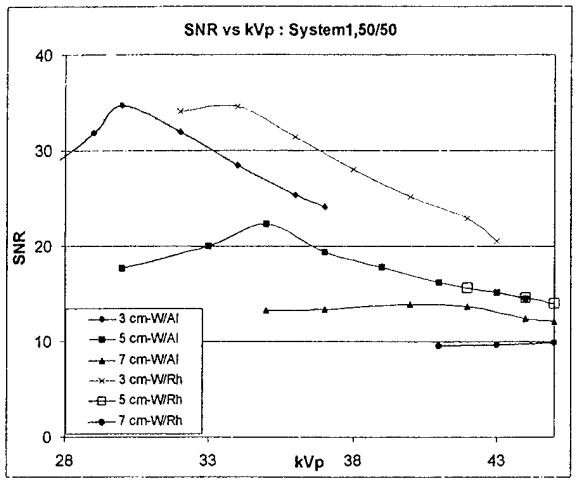

Figure 7: System 1, SNR vs. kVp.

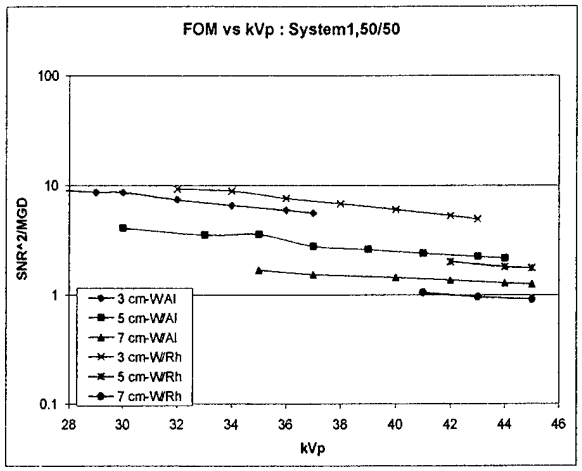

Figure 8: System 1, FOM vs. kVp.

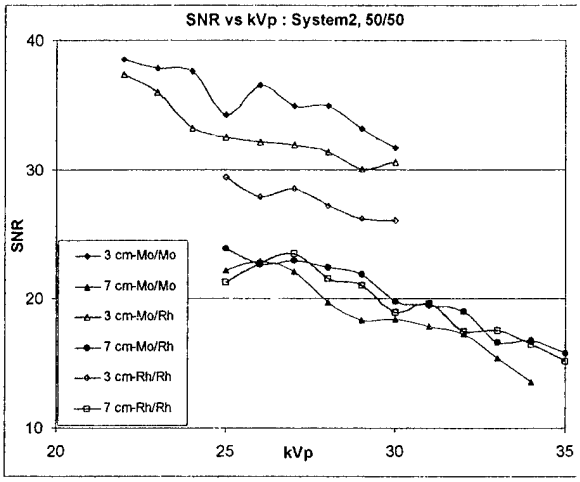

Figure 9: System 2, SNR vs. kVp. 5 cm phantom data have been omitted for clarity, and fall between the 3 cm and 7 cm phantom data shown.

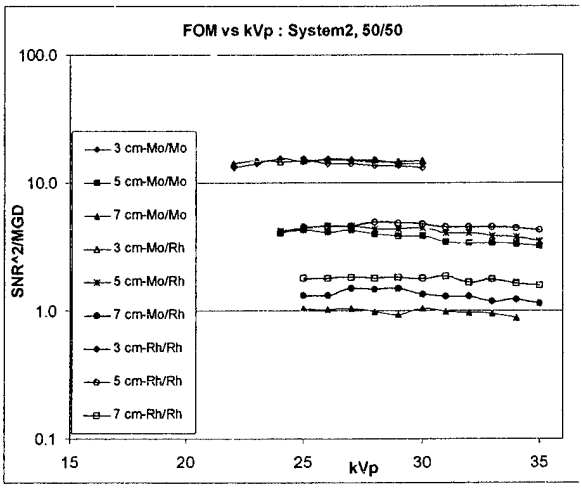

Figure 10: System 2, FOM vs. kVp.

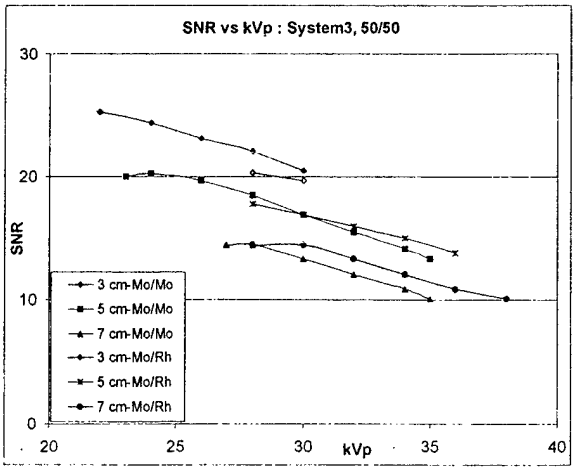

Figure 11: System 3, SNR vs. kVp.

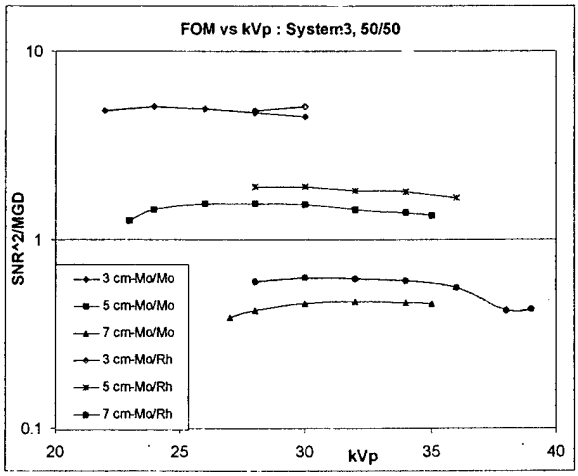

Figure 12: System 3, FOM vs. kVp.

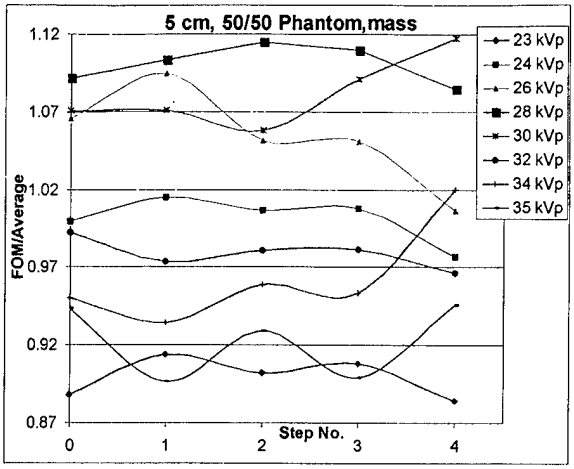

Figure 13: FOM values for the five steps of the mass stepwedge, normalized by the average value for each step. The average FOM values ranged from 0.2 (step 0) to 0.011 (step 4). Data are from System 3, imaging the 5 cm 50/50 phantom.

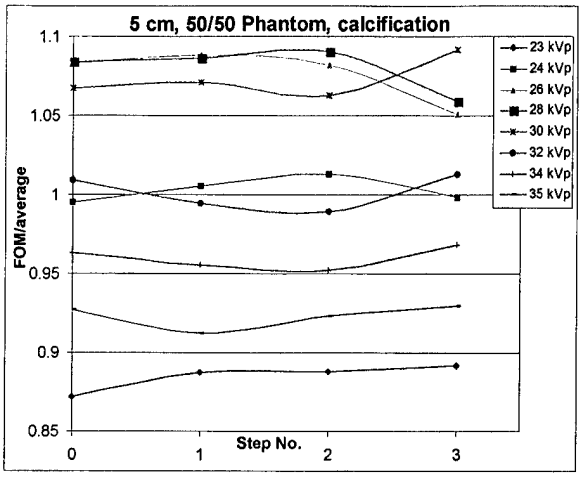

Figure 14: FOM values for the four steps of the calcification stepwedge, normalized by the average value for each step. The average FOM values ranged from 1.4 (step 0) to 0.64 (step 3). Data are from System 3, imaging the 5 cm 50/50 phantom.

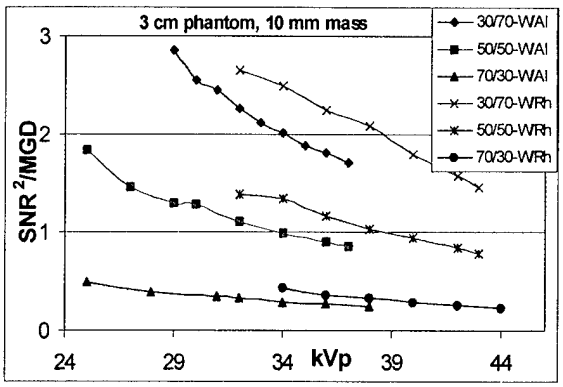

Figure 15: FOM vs kVp for 3 cm thick phantoms of three compositions, imaged on System 1.

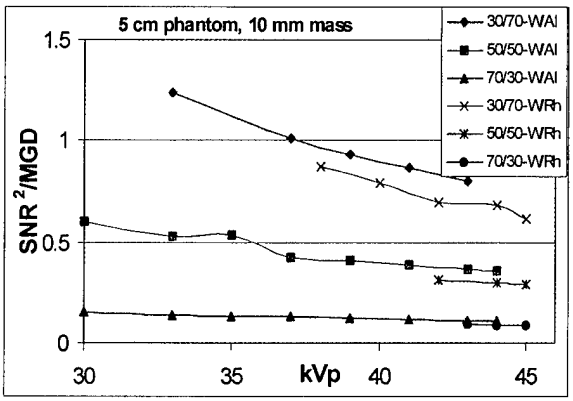

Figure 16: FOM vs kVp for 5 cm thick phantoms of three compositions, imaged on System 1.

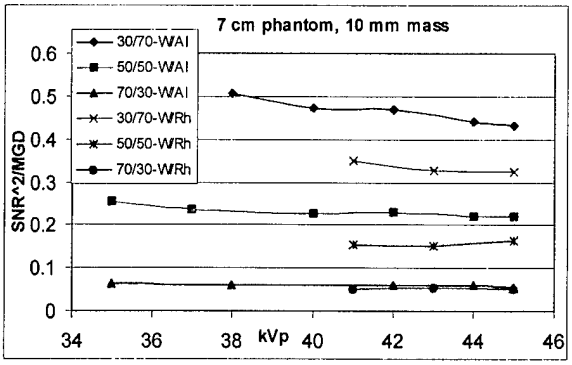

Figure 17: FOM vs kVp for 7 cm thick phantoms of three compositions, imaged on System 1.